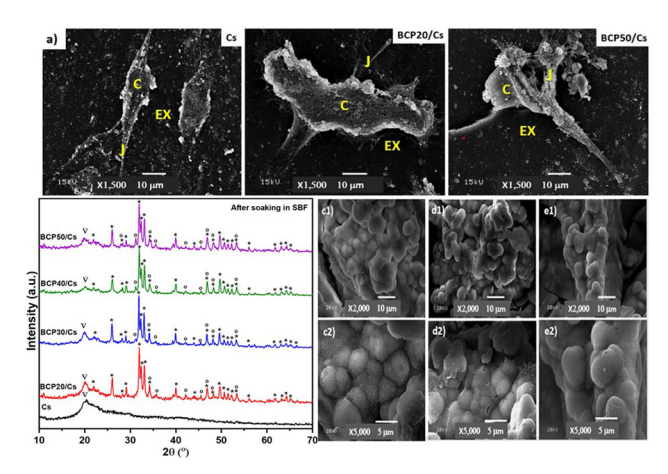
Research Article

Lila A. Al-Khattaby, Islam E. Soliman*, Mohamed A. Aboelnasr, and Samah S. Eldera

In vitro study of the biphasic calcium phosphate/chitosan hybrid biomaterial scaffold fabricated via solvent casting and evaporation technique for bone regeneration

https://doi.org/10.1515/ntrev-2023-0149 received July 16, 2023; accepted November 2, 2023

Abstract: Biphasic calcium phosphate (BCP)/chitosan (Cs) composites (BCP/Cs) were assessed for reinforcement in vitro bone regeneration. BCP ceramics have been used to overcome the limitations of single-phase biomaterials. In this study, composite samples were prepared using solvent casting and the evaporation technique. The BCP powder at different concentrations (20, 30, 40, and 50%) was added to the Cs solution to obtain the composite samples. The morphologies and physicochemical properties of the prepared composites were investigated using physical methods. The biocompatibility of composites (BCP/Cs) was studied in vitro by immersion in simulated body fluid. Additionally, the cytotoxicity and viability of the composite samples were evaluated. The results showed that the addition of BCP improves the apatite-forming ability and enhances the bioactivity and biomineralization of the BCP/Cs composites. The mechanical stability of the composite sample was improved essentially by the strong interaction between BCP and the Cs matrix. In addition, the higher the amount of BCP added (50 wt%), the higher the amount of adsorbed protein, and the suitable bioactivity of composites was enhanced. Furthermore, BCP/Cs composites boosted the cell viability and cell proliferation of normal human osteocyte cells. Hence, BCP/Cs composites could be an excellent alternative to bone implants in tissue engineering applications.



Graphical abstract

Keywords: chitosan, biphasic calcium phosphate, composites, biocompatibility evaluation

1 Introduction

Over the past few years, research efforts have been in progress in the field of bone grafts and other artificial implants. However, the ideal method for repairing bone deformities in orthopedics is autologous osteology. Although the best method for repairing bone deformities in orthopedics is still autologous bone, it has disadvantages including limited availability and the transmission of infections to the patient [1]. The available strategy for avoiding the defects of this treatment is bone tissue engineering due to its promising applications in clinical therapies [2]. One of the great challenges facing the field of tissue engineering is the design of biomaterials that are compatible with the surrounding biological environment. These biomaterials are used as substrates to deliver the appropriate cells and stimulate them to grow, reproduce, and form new tissues. This means that to obtain an ideal and suitable scaffold, it should mimic the

^{*} Corresponding author: Islam E. Soliman, Biophysics Branch, Physics Department, Faculty of Science, Al-Azhar University, Nasr City, 11884, Cairo, Egypt, e-mail: islamsoliman@azhar.edu.eg
Lila A. Al-Khattaby: Physics Department, Faculty of Science, King Abdulaziz University, Jeddah, Saudi Arabia
Mohamed A. Aboelnasr: Biophysics Branch, Physics Department, Faculty of Science, Al-Azhar University, Nasr City, 11884, Cairo, Egypt
Samah S. Eldera: Physics Department, Faculty of Science, King Abdulaziz University, Jeddah, Saudi Arabia; Physics Department, Faculty of Science, Al-Azhar University, Nasr City, Cairo, Egypt

natural components of the bone tissue to be regenerated [3]. In addition, these biomimetic materials should possess several properties, such as porosity, proper pore distribution, the ability to absorb over time, biodegradation, and finally, mechanical properties.

The extracellular matrix of bone is composed of organic and inorganic substances consisting of hydroxyapatite nanocrystals in type I and type III collagen fibers [4]. The organic material used in this study was chitosan (Cs), and the inorganic material was biphasic calcium phosphate (BCP). Cs is a partially deacetylated polysaccharide polymer (poly-1,4-p-glucosamine) from natural chitin, and its structure resembles glycosaminoglycans; therefore, it is commonly used in bone tissue engineering [5]. Cs is a natural polymer with excellent biodegradability by human enzymes, and its degradation products are non-toxic [6]. It can be easily molded into different forms because it is a flexible polymer and therefore does not have the mechanical strength of natural bone [7]. As a result, Cs scaffolds alone cannot mimic all the requirements of bone tissues [8]. Despite all the above properties of Cs, its bioactivity is low and needs to be improved, like other polymers. Therefore, efforts have been made previously to develop polymeric Cs matrixes reinforced with nano-reinforced fillers, such as calcium phosphate compounds, to obtain scaffolds with improved bioactivity and suitable mechanical properties [9]. Therefore, one of the calcium phosphate compounds, like BCP, was selected and added to Cs to control its properties and obtain suitable mechanical and biological properties for implantation.

The reason for choosing BCP is that it combines two different crystalline phases, namely, hydroxyapatite phase (HA) and tricalcium phosphate phase (TCP) (HA/TCP) at an appropriate ratio to overcome the problems of single-phase HA such as poor biodegradation rate and low mechanical stability [10,11]. However, to manage this problem, BCP can provide a product with controlled bioactivity and biodegradation at a balanced rate with high mechanical stability [12]. Since BCP is an inorganic compound with bioactivity on the surface, its preparation with physical properties, such as surface area, particle size, and morphology, can improve the speed of bone healing. Thus, its preparation in the nanoscale range is preferable. BCP can also form intercalated structures with polymer matrices. Nevado et al. [13] reported that PLA/BCP composites produced self-induced intercalated layers of polylactic acid. Some previous works [14-18] have been devoted to studying the effect of adding different proportions of Cs polymer to calcium phosphate compounds. Gan et al. [14] studied the effect of different proportions of Cs on BCP to create scaffolds containing arginine-glycine-aspartic acid peptide and found that Cs increased cell attachment, spreading, and osteogenic differentiation. Cs-based fluorohydroxyapatite bioceramic with injectable hydrogel-containing cells, prepared by Cheng et al., demonstrated highly acceptable biological and mechanical properties [15]. Also, Abd-Khorsand et al. produced porous three-dimensional scaffolds composed of HA-poly(acrylic acid)-Cs-TiO₂ using the freeze-drying technique that showed an improvement in cell growth and proliferation [16]. Further, Sendemir-Urkmez and Jamison [17] investigated the effect of 25 wt% BCP powder added to Cs, prepared by the freeze-drying technique, on the differentiation of osteogenic cells and showed an improvement in osteoconductivity in polymeric scaffolds. However, no study has documented the effect of adding high proportions of calcium phosphate to Cs polymers to manufacture a scaffold with high biocompatibility. Therefore, this study aims to fabricate composite scaffolds based on BCP/Cs with high BCP additives prepared via solvent casting and evaporation technique to evaluate their effect on the mechanical strength, cell adhesion, and bioactivity of composite scaffolds.

In the present study, BCP particles were synthesized by the coprecipitation method, and BCP/Cs composite scaffolds were fabricated *via* solvent casting and evaporation technique. The physicochemical, mechanical, and biological properties of the prepared BCP/Cs composites were studied and compared with those of pure Cs. Moreover, their capability of biomineralization and protein adsorption was investigated by *in vitro* testing in distilled water, simulated body fluid (SBF), and phosphate-buffered saline (PBS), respectively. The cytotoxicity and cell viability of the prepared composites were tested in human osteocytes (normal cells) to evaluate their ability to activate bone growth and integration.

2 Materials and methods

2.1 Materials

Calcium nitrate tetrahydrate (Ca(NO₃)₂·4H₂O), ammonium dihydrogen phosphate ((NH₄)H₂PO₄), ammonium hydroxide (NH₄OH), Cs (C₅₆H₁₀₃N₉O₃₉) with a molecular weight of 1526.5 g/mol and N-deacetylation degree of 85%, nitric acid (HNO₃), and acetic acid (96%) were bought from Sigma-Aldrich, St. Louis.

2.2 Preparation of BCP

BCP with a Ca/P ratio (1.60) was prepared using a wet chemical co-precipitation technique, as reported by El-Gohary *et al.* [19], with few modifications. In detail, 37.79 g of Ca $(NO_3)_2$ ·4H₂O as a source of Ca was dissolved in 1,000 mL of deionized water, and 13.98 g of $(NH_4)H_2PO_4$ as a source of P was dissolved in 1,000 mL of deionized water. The pH of

each aqueous solution was adjusted to 6 by the addition of dilute NH₄OH or HNO₃ solutions when required. (NH₄)H₂PO₄ solution was slowly added from a burette in a dropwise manner (2-5 mL/min) into a stirred Ca(NO₃)₂·4H₂O solution maintained at (60°C) on a hot plate during mixing. When dropping was completed, the temperature of the mixture was raised to the boiling point at 100°C for 2h with continuous stirring in a sealed container. Thereafter, the obtained slurry was left overnight without stirring until it cooled and formed a white precipitate. After 24 h, the white precipitate was filtered from the suspension, rinsed three times with deionized water to a neutral pH, and dried in an oven at 100°C in the air overnight. The dried powder was sintered at 1,100°C in an air atmosphere for 2 h to achieve BCP [20]. The sintered powder was deagglomerated using stainless steel sieves to obtain particles with a size of 40 µm.

2.3 Fabrication of BCP/Cs composite scaffolds

The prepared composites were synthesized using solvent casting and evaporation techniques. Initially, the Cs solution was prepared by dissolving a fixed weight of Cs powder (1g) in 100 mL of acetic acid solution (1% w/w) while stirring for 4 h to obtain a perfectly transparent solution. Four different concentrations of BCP powder, 20, 30, 40, and 50%, were added to the Cs solution and stirred for 2h to ensure a better distribution (homogeneity) of BCP particles in the composite scaffolds. After that, the solution was cast in a well plate and aged in an oven at 50°C for drying. The samples were then subjected to alkali treatments by soaking them in 1 mol/L NaOH aqueous solutions to raise hydrophilicity and crystallinity [21]. Finally, the samples were rinsed with deionized water and air-dried. The obtained Cs was denoted as a control sample, and BCP/Cs composites (20, 30, 40, and 50%) were denoted as BCP20/Cs, BCP30/Cs, BCP40/Cs, and BCP50/Cs composites, respectively.

2.4 Characterization of composites

2.4.1 XRD analysis

The prepared BCP powder, Cs, and BCP/Cs composites were analyzed by XRD using a Bruker Axs D8 ADVANCE diffractometer, operating at 40 mA and 40 kV with CuKα radiation (λ = 1.54056 Å) in the 2θ (10–70°) with a 0.02° step size and 0.05 s.

2.4.2 Fourier transform infrared (FTIR) analysis

FTIR spectroscopy was performed using an FTIR spectrophotometer (Demonstrate 1600, Perkin-Elmer Co. USA) to identify the chemical functional groups of the prepared composites. The prepared samples were completely dried, then well pulverized and mixed with potassium bromide (KBr) with a 1:100 weight ratio (specimen/KBr), which was compressed uniaxially in an evacuated die to form a pellet. The FTIR spectra were collected in the range between 4,000 and 400 cm⁻¹ with a resolution of 2 cm⁻¹.

2.4.3 Scanning electron microscopy (SEM)

The surface morphology of the prepared samples before and after soaking in SBF was measured using an SEM (model XL30, Philips) at an acceleration voltage of 30 kV. SEM micrographs were obtained after covering the specimens with a gold layer to obtain an excellent view using Edwards 5150 sputter coating, England. The SEM was equipped with an energy-dispersive X-ray spectroscope (EDS) to identify the chemical elements in the prepared samples.

2.4.4 Analysis of mechanical properties

The mechanical properties of the developed composites were assessed by calculating Young's modulus and stiffness using a TA.XT plus Stable Texture Analyzer (Stable Micro Systems, Surrey, UK). The samples were prepared for mechanical testing by evenly cutting them to form sheets with a gauge length (30 mm) and width (10 mm). The composite samples were located between two compression plates using an EMIC DL3000 testing machine and pressed at a constant speed of 2 mm/min. A load cell of 500 N was used at ambient RT. The statistical analysis of the calculated data was performed with an ANOVA program using three replicates per sample type.

2.5 In vitro bioactivity in SBF

In vitro bioactivity of the composite samples was carried out by evaluating the apatite forming-ability on their surface after soaking in SBF solution. The prepared samples were soaked in SBF at 37°C according to the method suggested by Kokubo and Takadama [22]. Each sheet of the composite sample of equal weight and shape with a specific surface-to-volume ratio (=0.1 cm⁻¹) was soaked in 60 mL of SBF solution and stored in an incubator (shaking water bath) at 37°C and pH = 7.4 for 15 days. After 15 days of soaking, the samples were retrieved from the SBF, placed on filter paper, slightly rinsed with distilled water and acetone, and dried in air at room temperature.

2.6 Protein adsorption analysis

The composite samples were incubated in PBS containing 2 mg/mL bovine serum albumin (BSA) and aged in a static thermos-incubator for different times determined before (30 min, 1, 3, 6, 9, and 12 h). After the predetermined periods, composite samples were completely rinsed with PBS and rinsed three times with deionized water to extract the non-adsorbed protein. After that, the rinsed samples were aged for 1 h at RT. The gradual reduction in BSA concentrations was calculated using a UV/V spectrophotometer (Jenway 4600, England) at 595 nm. The amount of protein adsorbed was measured with a calibration curve by comparing the absorbance values of the aliquot solution based on the following equation [23]:

$$Q = (C_{\rm i} - C_{\rm f})V/M, \tag{1}$$

where Q is the adsorbed amount of protein (mg/g), C_1 is the initial protein concentration (mg/mL), C_f is the remaining protein concentration in the PBS solution after removing the sample from it (mg/mL), V is the total volume of the PBS solution (mL), and M is the weight of the composite sample added to the solution.

2.7 In vitro cell culture analysis

Newly manufactured scaffolds that had been exposed to cellular cytotoxicity were assessed on human osteocytes (normal cells). The positive control in this experiment was doxorubicin. The composite sample was dissolved in 20% dimethyl sulfoxide (DMSO) at a concentration of 1 mg/mL.

The cytotoxic activity of the tested substances was carried out using the SulfoRhodamine-B (SRB) trial toward normal cells (human osteocytes). This cell line was purchased from the VACSERA-Cell Culture Unit, Cairo, Egypt. DMSO, SRB, and RPMI-1640 medium reagents were obtained from Sigma Company (St. Louis, USA). Fetal bovine serum was purchased from GIBCO, UK. A mixture consisting of RPMI-1640 medium with 10% fetal bovine serum and antibiotics (streptomycin 100 mg/mL and penicillin 100 units/mL) was added. The cells were grown in a humidified incubator in a CO₂ atmosphere (5% v/v) at 37°C. In a 96-well plate, the cells were cultured at a density of 1.0×10^4 cells/well for 48 h at 37°C and 5% CO₂. After completion of the incubation period, the cultured cells were incubated with the prepared samples for 3 and 7 days. Finally, the treated cells were compared with untreated control cells.

Triple wells were prepared for each dose. The media were removed, and the cells were fixed with 10% trichloroacetic acid

(TCA) at 150 mL per well at 4°C for 1 h (SRB protein binding was reduced by TCA). The cells were washed three times with distilled water. At RT, the cultured cells were stained with 70 mL/well of 0.4% SRB for 10 min (in a dark place). The cells were washed with 1% glacial acetic acid to remove excess dye. The plates were air-dried for 24 h. With 50 mL/well of 10 mM tris base (pH 7.4), the dyes were dissolved for 5 min on a shaker at 1,600 rpm. At 570 nm, using an ELISA microsheet reader (EXL 800 USA), the optical density was measured for each well. Using the equation (100 \times A₅₇₀ of the sample treated with the tested materials/A₅₇₀ from the sample untreated with the tested materials), cell viability was calculated as a percentage, and IC₅₀ (the least concentration desired to induce 50% of cell death after exposure to samples) values were measured using the origin program [24].

2.8 Statistical analysis

All collected data were presented in triplicate and given as mean \pm standard deviation. The statistical analysis was performed by one-way ANOVA using Excel (Microsoft Office, 2016). The p < 0.05 value was considered a significant difference between groups.

3 Results and discussion

3.1 XRD analysis before soaking in SBF

The XRD patterns of pure Cs and pure BCP, compared to different BCP/Cs composites, are shown in Figure 1. As shown in the figure, there is a broad halo around $2\theta = 20^{\circ}$, indicating that Cs has an amorphous structure, although there is a diffuse peak around $2\theta = 20^{\circ}$. According to a recent study by Karava *et al.* [25], this diffuse peak indicates some degree of ordered alignment of the polymer chains. Also, Figure 1 shows XRD patterns of pure BCP after sintering at 1,100°C. This pattern shows diffraction peaks assigned to two different crystalline phases: HA phase and β -TCP phase.

Four peaks appeared at 2θ values of 25.8°, 31.7°, 32.1°, and 32.9°, which indicated the (0 0 2), (2 1 1), (1 1 2), and (3 0 0) planes, respectively. These peaks can be assigned to the HA phase according to the standard JCPDS file no. 9-432. On the other hand, there are some lower diffractions at 2θ values of 27.7°, 31°, and 34.3°, which are indicated by (2 1 4), (2 1 0), and (2 2 0) planes, respectively. These peaks can be assigned to β -TCP according to the standard JCPDS card no. 70-2065.

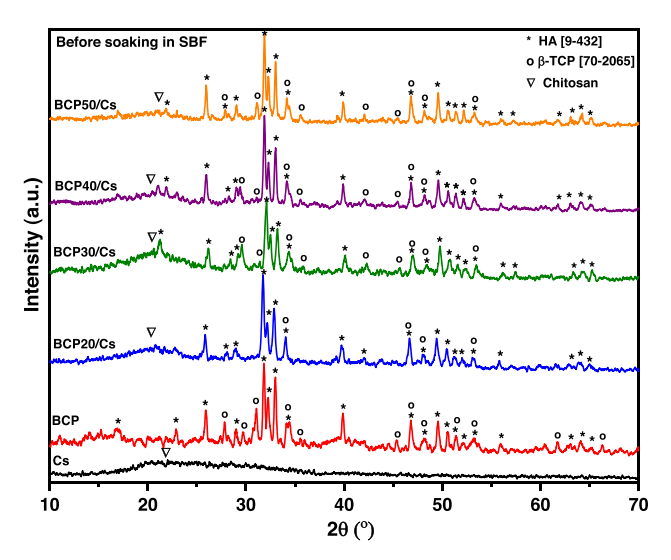


Figure 1: XRD patterns of Cs, BCP, and BCP/Cs composites with different BCP 20, 30, 40, and 50% contents; (∇) for Cs (*) for HA and (o) for β -TCP.

The presence of these two phases, HA and β -TCP, in the same sample, indicates the formation of BCP [20].

The phase compositions of BCP/Cs composites are shown using the XRD pattern in Figure 1. The broad diffraction peak of Cs was at around $2\theta = 20^{\circ}$ side-by-side, with sharp diffraction peaks of the BCP crystalline phase confirming the presence of Cs in the composite matrix [26]. XRD patterns illustrated that with the addition of BCP, the diffraction peak at 20° became broader and flatter, but the diffraction peaks ascribed to HA and β-TCP appeared to be more distinguishable in BCP/Cs composites [27]. Moreover, the diffraction peaks of HA at $2\theta = 32.2^{\circ}$ show a higher degree of splitting with increased addition of BCP, especially when the BCP content reaches 50%. The crystallite size (D) of both pure BCP and the BCP/Cs composite was calculated from a characteristic peak at 25.9° (0 0 2) corresponding to the HA phase using Scherrer's equation [28], that is, $D = 0.9\lambda/(\beta_{002} \cos \theta)$, where *D* is the crystallite size (nm), λ is the wavelength of the X-ray (0.154178 nm), β_{002} is the full-width at half-maximum intensity (rad) of the (0 0 2) peak, and θ is Bragg's diffraction angle. The results of the crystallite size of all samples are listed in Table 1. The crystalline sizes of all prepared samples are in the range of 30-43 nm. This indicates that the HA in the pure BCP and BCP/Cs composites are nano-sized crystals. Moreover, it can be observed that the crystallite size of HA in pure BCP is larger than in BCP/Cs composites, and the higher the BCP content, the larger the crystallite size [29].

The amount of crystalline HA phase in the investigated volume of BCP or BCP/Cs composite samples was measured by the crystallinity index (CI_{XRD}). The CI_{XRD} of the prepared samples was calculated from XRD patterns by the following

Table 1: Crystallite size (D) calculated using the Scherrer equation and the CI_{XRD} and CI_{FTIR} values obtained from the XRD patterns and FTIR spectra

Samples	<i>D</i> (nm)	Crystallinity indices			
		Before soaking		After soaking	
		Cl _{XRD}	CI _{FTIR}	Cl _{XRD}	CI _{FTIR}
BCP pure	43.27	0.84	3.01		
BCP20/Cs	30.47	0.65	2.23	0.61	2.05
BCP30/Cs	32.96	0.71	2.4	0.68	2.08
BCP40/Cs	35.22	0.79	2.55	0.71	2.13
BCP50/Cs	38.74	0.81	2.62	0.65	2.07

empirical equation: $CI_{XRD} = 1 - [V_{112/300}/I_{300}]$ proposed by Landi *et al.* [30] by drawing a baseline from $2\theta = 30$ to 35° and then measuring the intensity of the hollow $(V_{112/300})$ between (3 0 0) and (1 1 2) reflection peaks and dividing the peak intensity (I_{300}) of (3 0 0) at 2θ = 32.2°. As shown in Figure 1 and listed in Table 1, the CI_{XRD} of all BCP/Cs composites is lower than pure BCP, confirming the occurrence of a potential interaction between the Cs chain and BCP particles. In addition, the main diffraction peak of β -TCP at 31.04° disappears in the BCP/Cs composite. This can be attributed to the use of acetic acid during the preparation of the BCP/Cs composite. Acetic acid can partially dissolve β-TCP and HA crystals, causing decreases in their CI_{XRD} and thus reducing the crystallite size of HA in the BCP phase [31]. Consequently, the dissolution process becomes relatively stronger because of the low content of the BCP, corresponding to the reduction in their crystallite size [32]. The obvious decrease in the crystallinity of BCP/Cs composites is specifically advantageous, where, based on previous results, calcium phosphate ceramics with lower crystallinity features are better in bone reconstruction. They are similar to natural bone with low crystalline features and have higher solubility rates than calcium phosphate ceramics with higher crystallinity [33].

3.2 FTIR analysis before soaking in SBF

Figure 2 shows the FTIR absorption spectra of Cs, BCP, and BCP/Cs composites. As shown in Figure 2, the spectral range has been divided into two regions: 400–1,750 and 2,750–4,000 cm⁻¹. These two regions have the main vibrational bands for Cs and BCP. The absorption bands are observed in the spectra of pure Cs, including those at 895 and 1,155 cm⁻¹ (C–O–C stretching vibration in the saccharide structure) [34], ~970–1,100 cm⁻¹ (C–O stretching model,

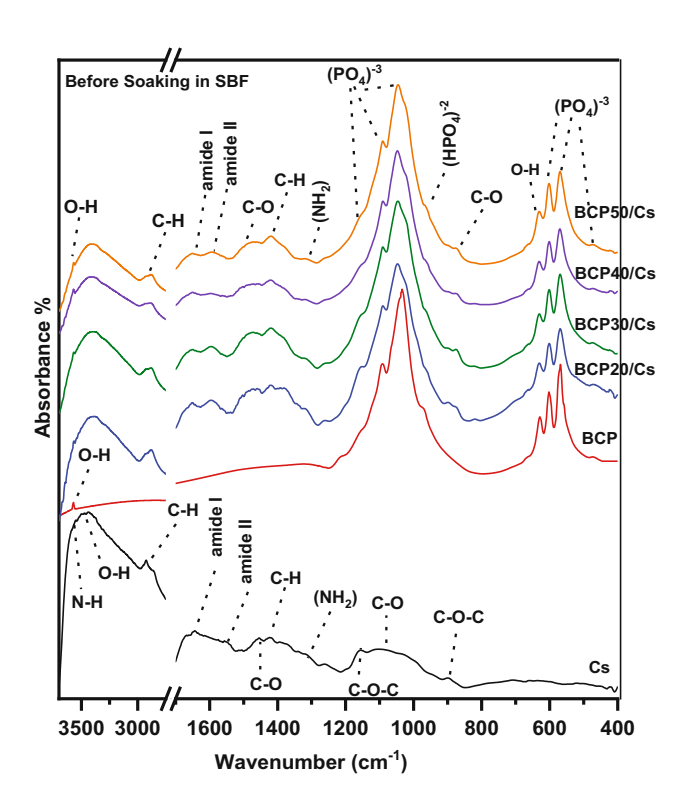


Figure 2: FTIR spectra of Cs, BCP, and BCP/Cs composites with different BCP contents (20, 30, 40, and 50%) before soaking in SBF.

~1,320–1,370 cm $^{-1}$ [amino (–NH $_2$)] [35], ~1,383–1,420 cm $^{-1}$ ((CH $_2$) symmetrical deformation), 1,450–1,470 cm $^{-1}$ (C–O stretching mode) [36], ~1,500–1,560 cm $^{-1}$ ((amine (–NH) deformation mode in amide II), ~1,600–1,700 cm $^{-1}$ (carbonyl (C=O) amide I stretching mode) [37], ~2,890–2,940 cm $^{-1}$ (methylene (–CH stretching mode)), and ~ 3,430–3,500 cm $^{-1}$ (O–H surface water and N–H stretching) [38]. All of these absorption bands represent the distinctive organic functional groups of Cs.

Also, Figure 2 shows the FTIR absorption spectrum of the pure BCP sample after sintering at 1,100°C. There are four vibrational bands corresponding to different modes of phosphate groups $[PO_4^{3^-}, HPO_4^{2^-}]$ [39]: ν_I band (P–O symmetric stretching) located at 964 cm⁻¹; ν_3 band (P–O antisymmetric stretching) around 976–1,000 cm⁻¹, which appears as triplet peaks located at 1,045, 1,092, and 1,156 cm⁻¹; ν_I band around 570–603 cm⁻¹, which appears as doublet peaks located at 570 and 603 cm⁻¹ (O–P–O bending mode); and ν_I band (P–O symmetric stretching) located at 472 cm⁻¹. These are specific bands for HA and ν_I -TCP [40]. Furthermore, there are two strong absorption bands located at 634 and 3,575 cm⁻¹ related to the hydroxyl group (O–H stretching mode) of HA in the prepared sample [10].

The two distinct functional groups that define the chemical composition of HA are the phosphate groups $[PO_4^{3-}]$ and the hydroxyl groups $[OH^{-}]$ but the distinctive functional

group that determines the chemical composition of $\beta\text{-TCP}$ is only the phosphate group. Consequently, the presence of these two groups in the same spectrum indicates that the synthetic BCP contained the HA and $\beta\text{-TCP}$ crystalline phases. On the other hand, the FTIR spectrum of the BCP/Cs composite shows the characteristic bands arising from both BCP and Cs. However, some absorption bands of Cs and pure BCP shifted and deformed. The characteristic band of amide II of Cs at 1,423 cm $^{-1}$ is shifted to a lower wavenumber at 1,413 cm $^{-1}$ in the BCP/Cs composite. Moreover, the characteristics of HPO $_4^{3-}$ at 974 cm $^{-1}$ in pure BCP is shifted to a lower wavenumber at 960 cm $^{-1}$ in the BCP/Cs composite.

As shown in Figure 2, the main characteristic bands of both Cs and BCP are present in all BCP/Cs composites, excluding slight band shifts and reduced intensity of some specific bands. For example, the intensity of the (-NH₂) band at 1,320 cm⁻¹ decreases with the higher contents of BCP. In addition, the typical vibration band of the PO₄³⁻ group at 471–650 cm⁻¹ became stronger and sharper while increasing BCP contents. According to FTIR data, the crystallization state of BCP and BCP/Cs composites can also be evaluated to determine whether or not it is affected by adding the BCP contents. This was done by measuring the crystallization index CI_{FTIR} of the phosphate band at 600 cm⁻¹ and its gradual splitting with the addition of BCP. The crystallization index (splitting factor] can be obtained by the following formula, $CI_{FTIR} = A + B/C$, proposed by Weiner and Bar-Yosef [41]. A baseline is taken from 490 to 650 cm⁻¹. The height of the double phosphate band was measured at 602 cm⁻¹ (A), 569 cm^{-1} (B), and the valley at 587 cm^{-1} (C) between 602 and569 cm⁻¹. As shown in Figure 2 and listed in Table 1, the CI_{FTIR} of all BCP/Cs composite samples is less than that of pure BCP.

These results suggest that there are some intermolecular interactions between BCP particles and Cs chains in all composite samples [42]. Therefore, the intermolecular interactions in Cs, such as H-bonding interactions within the network, become weaker with more BCP contents. Thus, it can be deduced that the incorporation of BCP powder interrupts the network formation. Moreover, the molecular chain of Cs acts not only as a matrix for the BCP powder but also anchors BCP powder in the structure and connects them to form composites [27].

3.3 Mechanical properties

To obtain composite materials that are used as scaffolds in bone tissue engineering, the criteria for initial mechanical properties must be taken into consideration at the

beginning. Referring to biomimetic approaches, the prepared composite scaffolds composed of degradable polymers (e.g., Cs) and BCP as an inorganic material aim to combine the flexibility of the polymer chain with the stiffness and strength of the filler material (ceramic) to improve the mechanical stability compared to a single component. The mechanical properties of the composite material can be described by measuring both Young's modulus and stiffness, especially for materials that are always subjected to compression and tension in only one direction [43]. This method is used to evaluate the ability of a composite to withstand changes when it is under compression or tension. Figure 3 shows the influence of BCP contents of 0, 20, 30, and 50 wt% on the mechanical properties of the composites. It can be seen that Young's modulus values for composites with 0, 20, 30, and 50 wt% BCP contents are approximately 0.8, 0.9, 1.1, and 1.7 GPa, respectively, with 50 wt% of BCP content having significantly more strength than pure Cs (p < p0.05) (Figure 3(a)).

A similar trend was also observed in all composite samples, with the stiffness values largely improving as the quantity of BCP increased (0.041, 0.067, 0.069, 0.086, and 0.13 MPa), respectively (p < 0.05) (Figure 3(b)). These are associated with the addition of BCP powder to the Cs matrix, which appears from chemical interactions between the NH₂ groups in Cs and the Ca²⁺ in the BCP or between the NH₂ groups and PO₄³⁻ [44], as discussed in previous measurements. Thus, the mechanical stability of the composite sample is improved essentially by the strong interaction between the filler surface (BCP) and the polymer matrix (Cs). This is related to the decrease in the porosity of the composite and the construction of mechanical interlocking within the Cs

matrix [26,45]. Moreover, these results emphasize the uniform dispersion of BCP particles within the Cs matrix. These BCP particles have a notable influence on the optimization of the mechanical stability of the prepared composite.

3.4 XRD analysis after soaking in SBF

Figure 4 shows the XRD patterns of Cs and BCP/Cs composites after soaking in SBF for 15 days. For pure Cs, the main diffraction peak of Cs appears at $2\theta=20^\circ$ after soaking in SBF, and no diffraction peaks of a new apatite phase or CaP precursors are observed. As is known, the growth of the apatite layer on the surface requires nucleation sites. These sites reduce the surface energy of minerals, which helps them grow, but they are not available on pure Cs surfaces [43,46]. These results indicate that Cs without the addition of BCP cannot form apatite, proving that they are not biologically active [47,48].

For composites, all BCP/Cs composites have the characteristic peaks of Cs ($2\theta = 20^{\circ}$) and the characteristic peaks (at $2\theta = 25$ – 35° for the HA phase: $2\theta = 28.3^{\circ}$, 31° , 34.2° , and 46.8° for the β -TCP phase) of the BCP phase. Furthermore, no formation of other phases is found after soaking in SBF, as shown in Figure 4. In BCP30/Cs and BCP40/Cs, the main diffraction peak of β -TCP in the BCP phase at $2\theta = 31^{\circ}$ is observed again with low intensity after soaking. This is mostly due to the recrystallization of the β -TCP phase, whose ions were dissolved in the acidic Cs solution, and then when placed in SBF with a pH > 5 a reverse reaction occurred, and it was recrystallized again [31].

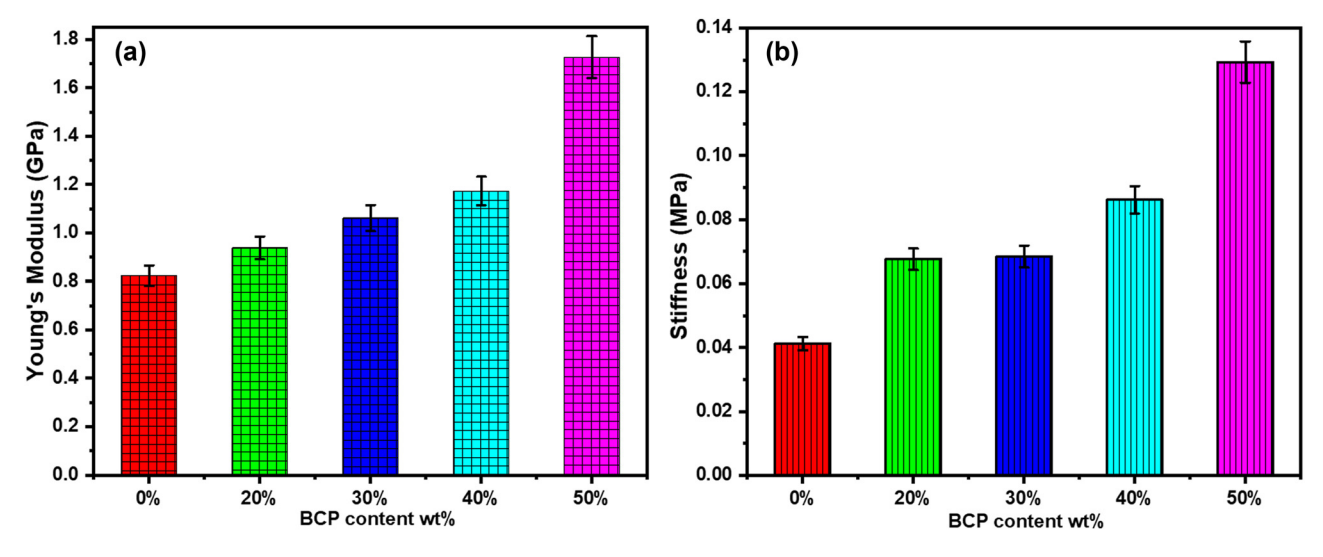


Figure 3: Young's modulus (a) and (b) stiffness of Cs and BCP/Cs composites containing different BCP contents.

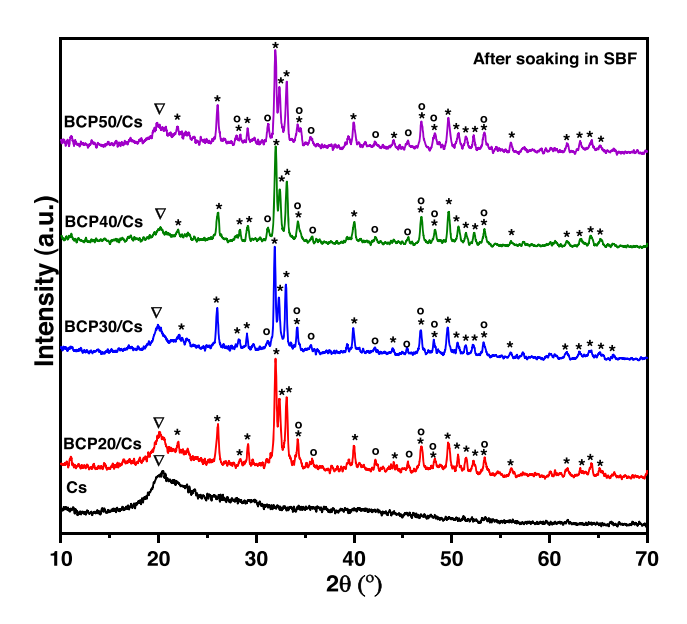


Figure 4: XRD patterns of Cs and BCP/Cs composites with different BCP contents (20, 30, 40, and 50%) after soaking in SBF.

The results of the CI_{XRD} of all composites after soaking in SBF are summarized in Table 1. The CI_{XRD} values of all samples decreased after soaking in the SBF solution compared to those before soaking. This decrease in CI_{XRD} is due to the initial dissolution of BCP and then re-precipitation to provide more apatite nucleation sites and form a calciumdeficient apatite layer on the composite surface. Hence, it indicates that the low crystallinity of the newly formed calcium-deficient apatite is responsible for the peak broadening of their diffraction patterns of the BCP/Cs composite [35]. The CI_{XRD} of these samples increases with an increasing amount of BCP, except for BCP50/Cs. The higher the BCP content present in the composite samples, the greater the number of nucleation sites, and the lower the surface energy of minerals, which leads to stimulating the growth of the apatite layer onto the surface. As a result, apatite formation on the composite surface has a high degree of crystallinity [49].

3.5 FTIR after soaking in SBF

FTIR spectra of pure Cs and BCP/Cs composites after soaking in SBF are presented in Figure 5. As shown in the pure Cs spectrum, the intensity of the absorption bands assigned to Cs decreased: C-O, -NH₂, and C=O. These changes indicate the hydrolytic degradation of the Cs matrix [50]. Moreover, no new absorption bands appeared on the surface of pure Cs after soaking in SBF. Consequently, the distinct function groups for apatite, such as PO₄³⁻ and OH⁻, were absent. The

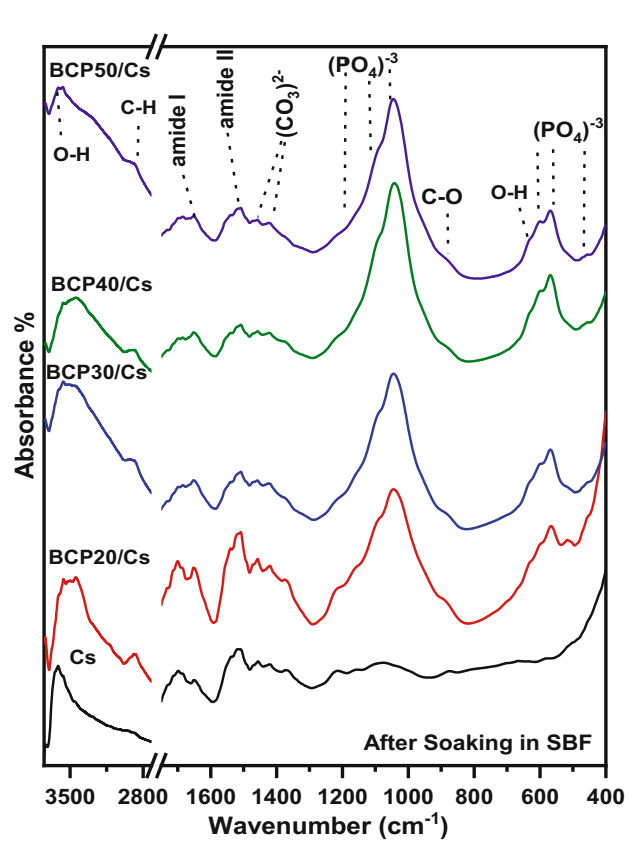


Figure 5: FTIR spectra of Cs and BCP/Cs composites with different BCP contents (20, 30, 40, and 50%) after soaking in SBF.

absence of a new apatite phase in pure Cs is due to the positive nature of its surface, resulting from the protonation of free amine ($-NH_2$) groups in Cs chains. This $-NH_2$ functional group tends to become ammonium cations [$-NH_3^+$] by dissolving Cs in acidic media, which in turn makes the whole Cs chain positively charged [51]. The positively charged Cs surface attracts the negatively charged chloride ions in the SBF solution, causing them to adsorb onto the surface. This impedes the formation of apatite nucleation sites, leading to the inhibition of the growth of apatite crystals [52]. This result proves that pure Cs cannot form an apatite layer on its surface.

As shown in Figure 5, for BCP/Cs composites, the characteristic bands of both Cs and BCP particles appear after soaking in SBF with noticeable changes. The intensity of the C–H (stretching mode) band at 2,890 cm⁻¹ decreased and became broader, while the C–H and N–H bands at 1,420 and 1,320 cm⁻¹, respectively, disappeared after soaking in SBF. This result suggests a partial degradation of Cs in composite samples, even after soaking in SBF [53]. Also, the carbonate (C–O) band at 1,450 cm⁻¹ resolved into two bands at 1,416 and 1,462 cm⁻¹ in all composites, indicating the incorporation of carbonate ions in apatite crystals. These results

DE GRUYTER

signify the formation of a large amount of hydroxycarbonate apatite layer (HCA) deposited on the BCP/Cs composite surfaces [54].

In addition, the OH $^-$ bands at 630 and 3,570 cm $^{-1}$ and PO $_4^{3-}$ bands at 567, 603, and 1,093 cm $^{-1}$ decreased and converted into bands with broadening shapes compared to before soaking. The obvious broadening of the P $^-$ O bands arises from the poor crystallinity and nanosize effects of BCP crystals [55]. This is demonstrated by calculating the CI $_{\rm FTIR}$ values of P $^-$ O bands around 600 cm $^{-1}$ after soaking in SBF, as shown in Table 1. The CI $_{\rm FTIR}$ of all the composite samples decreased after soaking compared to before soaking. This reduction in the CI $_{\rm FTIR}$ is due to the dissolution of PO $_4^{3-}$ ions, which are then substituted with CO $_3^{2-}$ ions in an apatite lattice to form AB-type HCA during the re-precipitation process [56].

Table 1 also shows that when the amount of BCP increased, the CI_{FTIR} values of the composites increased, except for a decrease in BCP50/Cs. As can be seen, the greater BCP content in composites leads to a slight increase in the splitting of the two P–O bands at 567 and 603 cm⁻¹, and hence, an increase in the CI_{FTIR} . This result indicates that the addition of BCP induces the formation of nucleation sites; thus, the negative charge increases on the composite's surface. Then, the apatite nuclei begin to grow by attracting the positively charged Ca^{2+} ions and then the negatively charged PO_4^{3-} ions in the surrounding solution [57]. Hence, it was confirmed that the addition of BCP improves the apatite-forming ability and enhances the bioactivity and biomineralization of the BCP/Cs composites.

3.6 Protein adsorption studies

Protein adsorption is one of the important parameters, as it helps the cell adhere to the implant surface. Figure 6 shows the amount of protein adsorption on the Cs and BCP/Cs composites up to 12 h of incubation in a BPS solution. It is seen that the amount of adsorbed protein increased with the increasing content of BCP in the Cs matrix. Therefore, the incorporation of BCP into the composites enhances the properties of the Cs network for protein adsorption and creates a local microenvironment on the composite surface rich in protein [58].

In general, protein adsorption is a complex process affected by several factors, such as surface roughness, electrostatic force, functional groups, and hydrophobicity [59]. Furthermore, BCP possesses two reactive sites, positive C-sites [Ca²⁺] and negative P-sites [PO₄³⁻], which work as

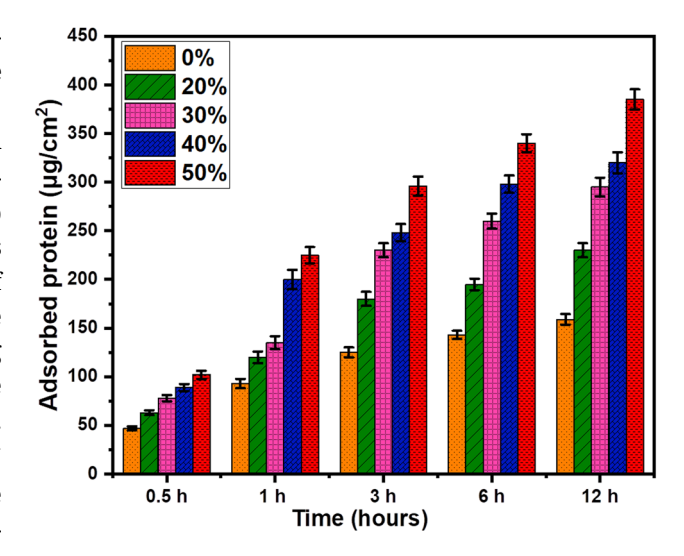


Figure 6: Protein adsorption profiles of Cs and BCP/Cs composites in PBS at 37°C for different incubation times.

binding sites for proteins and provide the main driving force for adsorbing proteins [60]. In this study, the exposed BCP nanoparticles on the Cs surface increased the binding or reactive sites of protein on composite surfaces and/or created an electrostatic interaction between protein molecules and the Cs surface, which in turn improved protein adsorption. Thus, all of these changes help increase the number of protein-binding sites on the composite surface.

3.7 SEM and EDS before and after soaking in SBF

Figure 7 shows the SEM micrographs of the Cs and the resultant BCP/Cs composite. The surface of pure Cs appeared to have a homogeneous microstructure with a smooth surface when compared with the BCP-loaded composite. The smooth surface of pure Cs (Figure 7(a)) changed and gradually disturbed the incorporation of BCP nanoparticles and became a rough surface (Figure 7(b)). A regular distribution of BCP nanoparticles on the surface of the composite was observed, which in turn increased the area of its outer surface. Furthermore, BCP nanoparticles appeared to be efficiently embedded in the polymer matrix due to the higher ionic cross-link density between BCP and the Cs network [61]. Figure 7(c) and (d) shows the EDS patterns of the Cs and BCP/Cs composites. The EDS pattern (Figure 7(c)) reveals that the chemical elements in this sample are [C, N, O] elements representing the basic chemical elements of Cs, but sodium [Na] may be caused by the remains of the NaOH solution used to neutralize the Cs sample. Furthermore, the

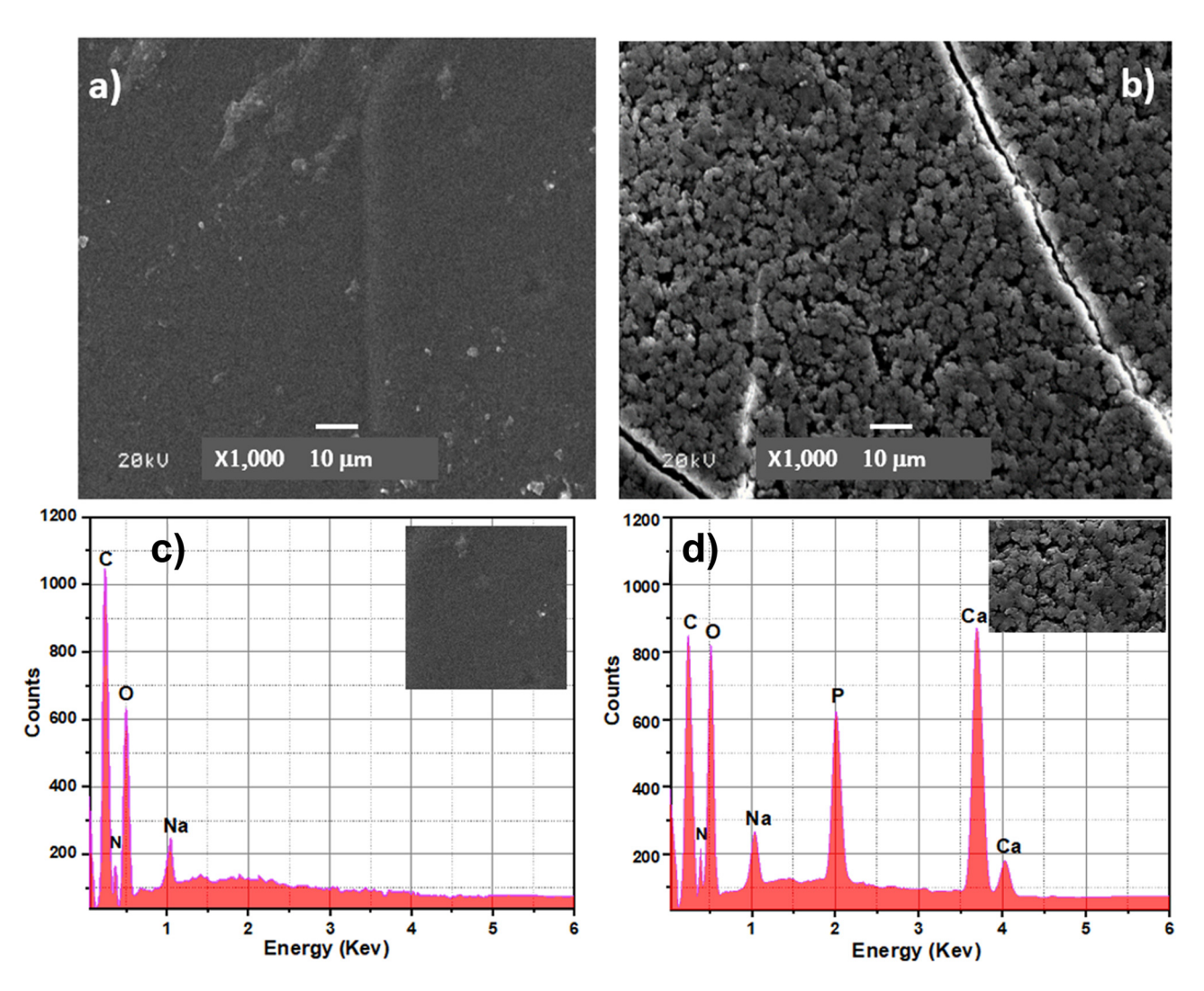


Figure 7: (a) SEM images of Cs, (b) SEM images of the BCP50/Cs composite, (c) EDS pattern of Cs, and (d) EDS pattern of the BCP50/Cs composite (before soaking in SBF).

EDS pattern (Figure 7(d)) illustrates that the BCP/Cs composite contains Ca and P elements as well as a Ca/P 1.55 ratio, originating from BCP along with [C, N, O] elements, where [O] originated from both components. These results confirm that the BCP powder is successfully incorporated into a polymer Cs matrix.

Figure 8 shows SEM images of the surface of pure Cs and of BCP/Cs composites after 15 days of soaking in the SBF solution. SEM images of pure Cs after soaking in SBF (Figure 8(a)) show small white particles on their surfaces. These particles resemble NaCl crystals that may have been precipitated from the SBF onto the Cs surface [62], as affirmed by the corresponding EDS pattern for the same sample, as shown in Figure 8(f). This indicates that pure Cs without any BCP addition is not bioactive [63].

Moreover, the composite surfaces are covered by bright tiny spherical particles with an average diameter of 4.6–5.5

μm, confirming the formation of the apatite layer [64] (Figure 8(b)–(e)). The number of spherical apatites deposited on the surface changed with the addition of different amounts of BCP contents. It is also clear that the surface of BCP20/Cs is not completely covered with the apatite layer. However, by comparing this with BCP30/Cs, there is an increased density of apatite layer amounts deposited on its surface, reaching full surface coverage in BCP50/Cs. Moreover, by observing the Ca and P peaks in the EDS pattern (Figure 8(g)) after soaking in SBF and comparing them to Figure 8(d) before soaking in SBF, it is found that there is a noticeable increase in Ca and P elements, indicating an improved formation of a dense apatite layer (mineral) on the BCP50/Cs composite surface [54].

This occurs due to the rough surface that appeared after the addition of BCP. In addition, the presence of these particles on the surface acts as a nucleation site and facilitates apatite crystal deposition [65]. The nature of the

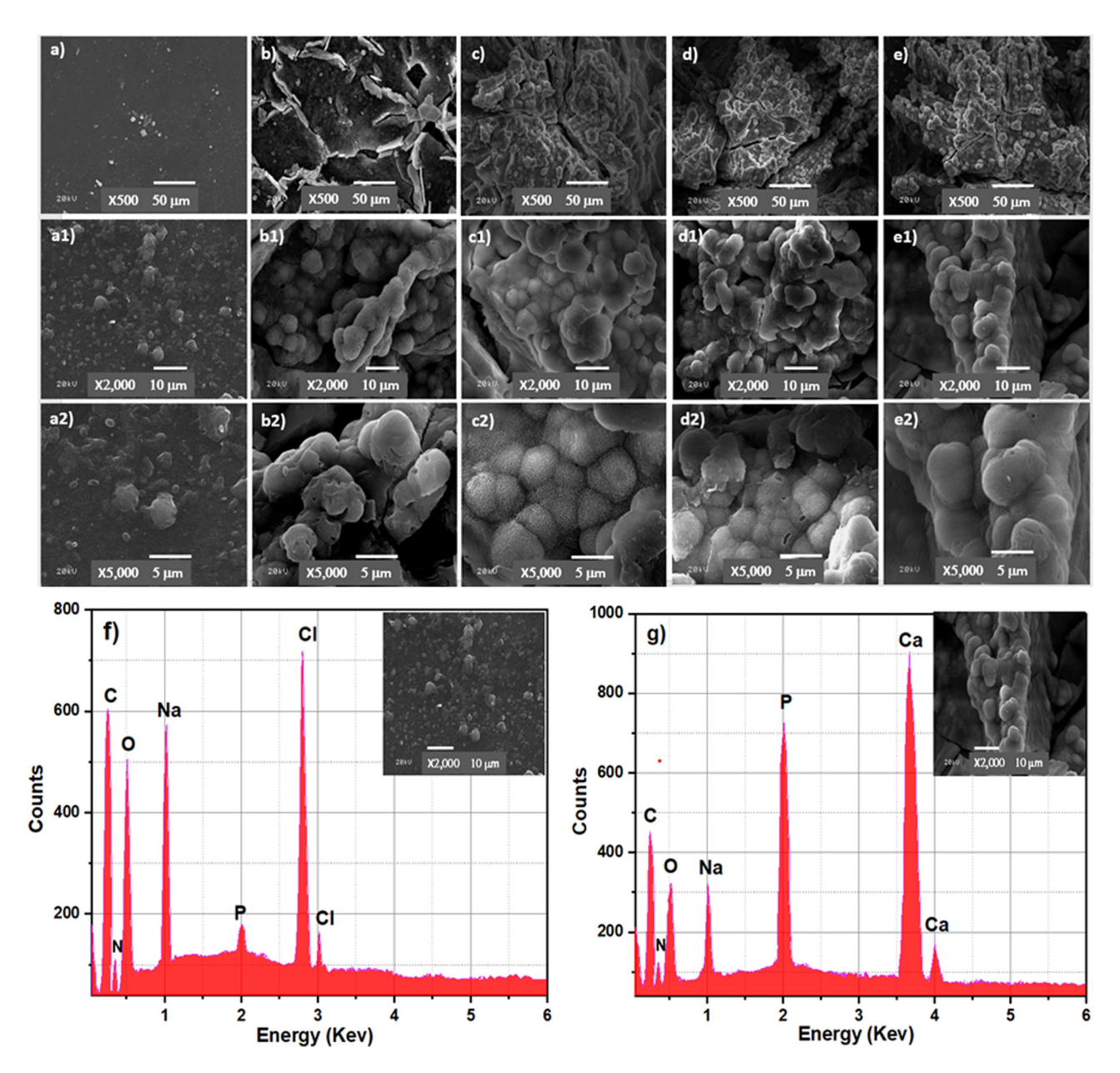


Figure 8: SEM images of Cs (a, a1, a2), BCP20/Cs (b, b1, b2), BCP30/Cs (c, c1, c2), BCP40/Cs (d, d1, d2), and BCP50/Cs (e, e1, e2) composites after soaking in SBF for 15 days; with different magnifications (×500, ×2,000, ×5,000) (f, g) EDS pattern of Cs and the BCP50/Cs composite after soaking in SBF for 15 days.

apatite layer is clear from the SEM imaging. The shape of the crystal and the cauliflower structure is likely typical of the formation of HCA observed, especially on the surfaces of BCP30/Cs and BCP40/Cs. This result confirms the good crystallization of the HCA layer on the surface of BCP/Cs composite samples.

The particle size distribution of the deposited apatite layer on all samples after soaking in SBF is shown in Figure 9. As can be seen from this figure, the average particle sizes of the apatite layer are about 5.5, 5.08, 4.9, and $4.6\,\mu m$ of BCP20/Cs, BCP30/Cs, BCP40/Cs, and BCP50/Cs, respectively. This is due to the addition of BCP in a larger proportion in BCP40 and BCP50, which increased the number of nucleation sites and their abundance on the surface and thus led to the small size of the apatite particles formed on the surface of these samples [66]. This indicates that these BCP particles play an important role in controlling the size of the apatite particles and thus controlling the biological interaction between the composite and the biological fluid.

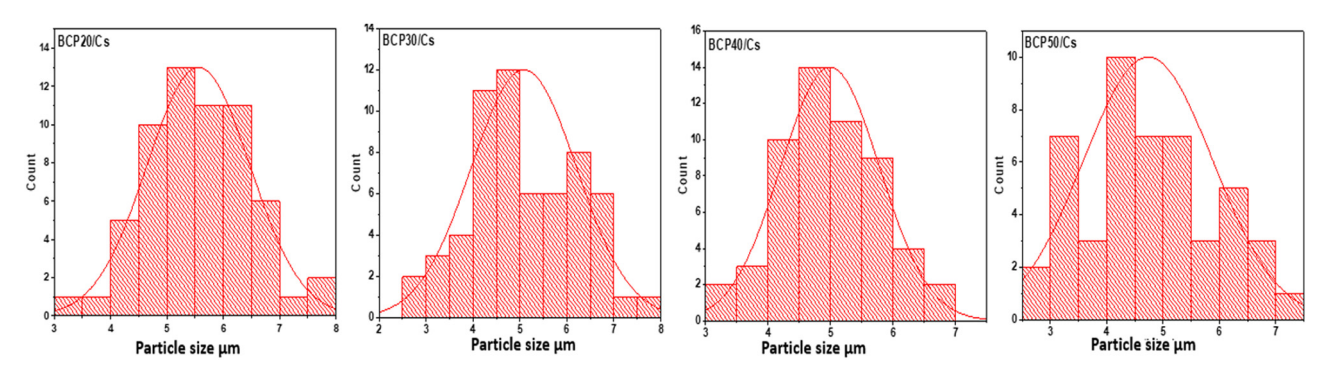


Figure 9: Particle size distributions of apatite layer formed on all composite samples.

3.8 In vitro cell culture analysis

The SRB assay was used to assess the safety of the composite samples for normal cells. The cytotoxicity of all prepared samples to normal human cells (osteocytes) was evaluated to examine the toxicity of these samples. The present study showed that most composite samples were non-cytotoxic ($IC_{50} > 130$ mM) on the human normal cell line. The cell viability assay showed that IC_{50} could not be

obtained. The toxicity values were less than 50% of the cell's validity ratio for different concentrations of scaffolds. This result indicates that the high proportions of the individual components of the prepared scaffolds (Cs and BCP) are characterized by their non-toxic properties, as mentioned before [49,67].

Furthermore, the morphology of cell attachment on the pure Cs, BCP20/Cs, and BCP50/Cs composites at 7 days of cell culture time was observed by SEM (Figure 10(a)).

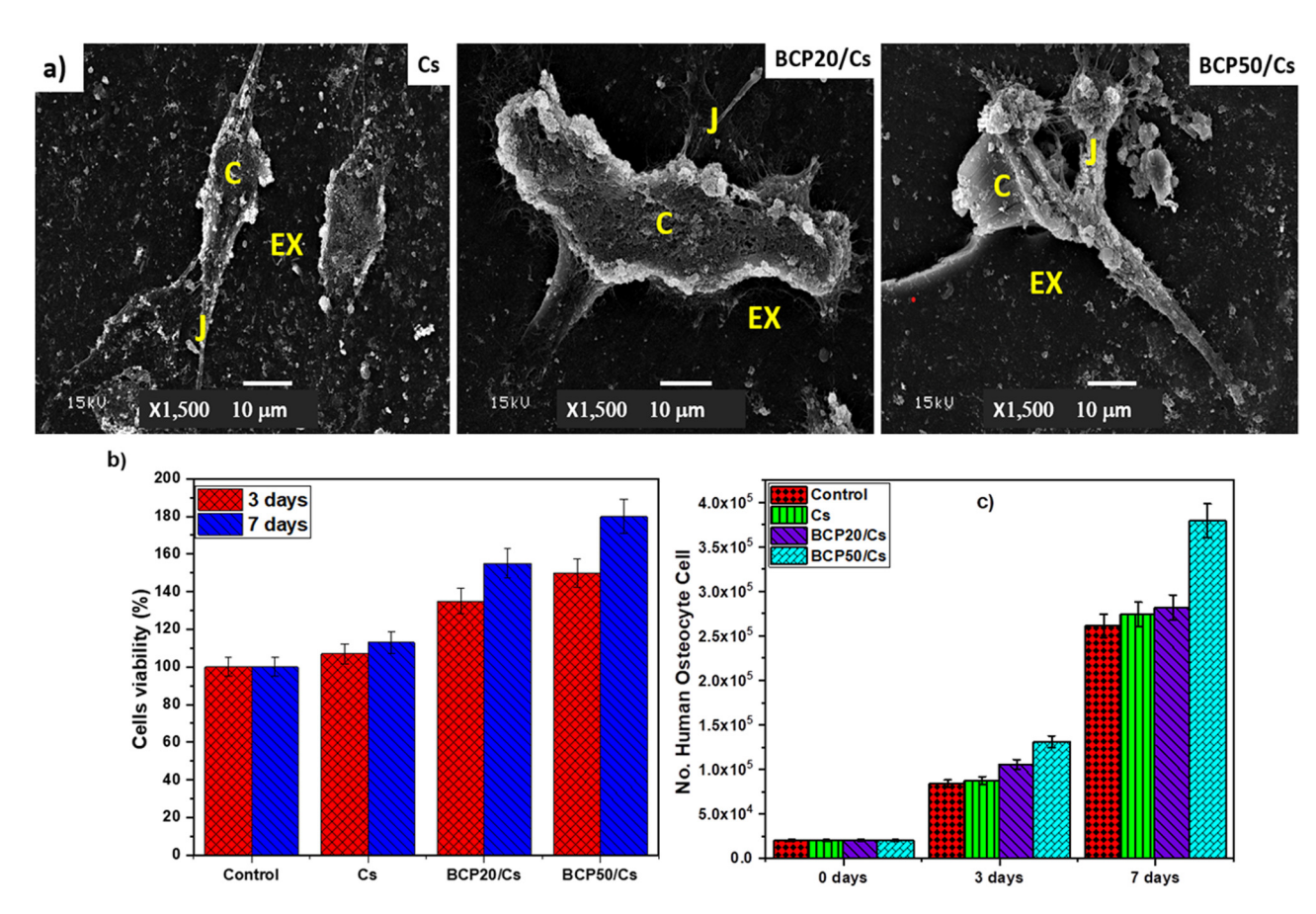


Figure 10: (a) SEM for normal human osteocyte after 7 days of cell culture; (b) cells viability assay; and (c) cell proliferation assay: Cells (C), cell–cell junctions (J), and extracellular matrix (EX).

SEM images showed that the normal human osteocytes cultured on pure Cs were in a segregated shape from the cells around them. On the other hand, normal human osteocytes were randomly spread over the composite surfaces and attached to the composite surfaces. There are cell-cell junctions extended between the cells within and above the composite matrix, which are quite evident. The joints and the extracellular matrix are very noticeable in the composite containing BCP, especially on the surface of BCP50/Cs (Figure 10(a)).

In addition, the growth of normal human osteocytes increases in the presence of BCP. This is due to an increase in the number of polar groups on the surface of the composite due to the addition of BCP, which thus helps to enhance the attachment of osteocyte cells. Moreover, the presence of a rough surface improves surface-wetting properties and thus has an indirect effect on cell attachment by stimulating the adsorption of serum proteins used for cell attachment [68]. Hence, the prepared composite with more BCP content is preferable for cell anchoring and attachment after 7 days, which may support osteogenic functions and bone regeneration.

Figure 10(b) and (c) shows significant differences in cell count after 3 and 7 days of incubation. As shown in the figure, there is an increase in the number of cells as follows: $8.7 \times 10^4 \pm 2.4$, $10 \times 10^4 \pm 1.8$, and $13 \times 10^4 \pm 2.3$ for Cs, BCP20/Cs, and BCP50/Cs samples, respectively, compared with control $8.4 \times 10^4 \pm 2.1$ after 3 days. But after 7 days, it was observed that there was a clear effect of these prepared samples on cellular proliferation by increasing the number of recorded cells as follows: $2.7 \times 10^5 \pm 1.7$. 2.8×10^5 \pm 2.3, and 3.7 \times 10⁵ \pm 1.4 for Cs, BCP20/Cs, and BCP50/Cs samples, respectively, compared with control $2.6 \times 10^5 \pm 1.8$. Therefore, the BCP50/Cs sample provides more safety with cells than BCP20/Cs and then Cs. These results assume that cell adhesion and growth are ruled by the presence of both Cs and BCP. In addition, this noticeable increase in cell attachment is a promising feature of BCP when it is added to Cs, where cell attachment is an essential factor for the growth, proliferation, and differentiation of various cell types, including human osteocytes. Recent studies have reported that BCP-based materials have the properties of stimulating bone formation in intramuscular sites early, which does not occur with HA or TCP [69]. These properties are due to the resorbability of BCP, which works to dissolve the CaP crystals; then, the HCA layer is precipitated near the adsorbing crystals. As a result, this mineralization, whether on the surface or within the pores, makes the composite (BCP/Cs) act as a scaffold for bone cell attachment and stimulates and accelerates bone formation [70].

4 Conclusion

Cs and BCP/Cs composites were successfully fabricated with the desired shape by solvent casting and evaporation technique. The structural, morphology, and chemical compositions of these prepared composites were analyzed by XRD, FTIR, EDS, and SEM. The physiochemical and biological properties of the BCP/Cs composite scaffold were studied, which showed the biocompatibility of this hybrid compound. The obtained results showed that mechanical properties, protein adsorption, and biomineralization (apatite formation) depend on the amount of BCP added. The higher the BCP content in the composite samples, the greater the growth of the apatite layer on the composite surface. FTIR spectra of all composites showed the presence of distinct organic (Cs) and inorganic (BCP) absorption bands. XRD and FTIR results exhibited that there is significant intermolecular interaction between BCP particles and the Cs chain, and an increase in the peak size of inorganic compounds was observed by increasing the BCP/Cs ratio. Furthermore, the incorporation of BCP into the Cs matrix increased Young's modulus and stiffness; therefore, these properties were controlled by adding BCP as a filler to make it suitable for cell adhesion and growth. In addition, protein adsorption results showed that the increase in BCP content increased the amount of protein adsorbed on a composite surface and the ability to form apatite. Furthermore, BCP/ Cs composites increased the cell adhesion and growth of normal human osteocyte cells. Therefore, choosing a scaffold with a high BCP content (BCP50/Cs) will be appropriate when used in areas with load-bearing osseous defects, such as the femur, which also require rapid healing. Hence, BCP/Cs composites could be an excellent replacement for bone implants in tissue engineering applications.

Acknowledgments: This project was funded by the Deanship of Scientific Research (DSR) at King Abdulaziz University, Jeddah(grant no. G: 236-247-1442). The authors, therefore, acknowledge the DSR for technical and financial support.

Funding information: This project was funded by the Deanship of Scientific Research (DSR) at King Abdulaziz University, Jeddah, (grant no. G: 236-247-1442).

Author contributions: All authors have accepted the responsibility for the entire content of this manuscript and approved its submission.

Conflict of interest: The authors state no conflict of interest.

References

- [1] Wang W, Yeung KW. Bone grafts and biomaterials substitutes for bone defect repair: A review. Bioact Mater. 2017;2(4):224–47. doi: 10.1016/j.bioactmat.2017.05.007.
- [2] Amini AR, Laurencin CT, Nukavarapu SP. Bone tissue engineering: recent advances and challenges. Crit Rev Biomed Eng. 2012;40(5):363–408. doi: 10.1615/CritRevBiomedEng.v40.i5.10.
- [3] Kar S, Kaur T, Thirugnanam A. Microwave-assisted synthesis of porous chitosan–modified montmorillonite–hydroxyapatite composite scaffolds. Int J Biol Macromol. 2016;82:82628–36. doi: 10. 1016/j.ijbiomac.2015.10.060.
- [4] Heng BC, Bai Y, Li X, Meng Y, Lu Y, Zhang X, et al. The bioelectrical properties of bone tissue. Anim Model Exp Med. 2023;6(2):120–30. doi: 10.1002/ame2.12300.
- [5] Li J, Tian X, Hua T, Fu J, Koo M, Chan W, et al. Chitosan natural polymer material for improving antibacterial properties of textiles. ACS Appl Bio Mater. 2021;4(5):4014–38. doi: 10.1021/acsabm. 1c00078.
- [6] Furko M, Balázsi K, Balázsi C. Calcium phosphate loaded biopolymer composites—a comprehensive review on the most recent progress and promising trends. Coatings. 2023;13(2):360. doi: 10. 3390/coatings13020360.
- [7] Nazeer MA, Yilgör E, Yilgör I. Intercalated chitosan/hydroxyapatite nanocomposites: promising materials for bone tissue engineering applications. Carbohydr Polym. 2017;175:17538–46. doi: 10.1016/j. carbpol.2017.07.054.
- [8] Ressler A. Chitosan-based biomaterials for bone tissue engineering applications: a short review. Polym. 2022;14(16):3430. doi: 10.3390/ polym14163430.
- [9] Vu BT, Hua VM, Tang T-N, Dang NN-T, Cao HT-T, Phan TB, et al. Fabrication of in situ crosslinking hydrogels based on oxidized alginate/N, O-carboxymethyl chitosan/β-tricalcium phosphate for bone regeneration. J Sci: Adv Mater Devices. 2022;7(4):100503. doi: 10.1016/j.jsamd.2022.100503.
- [10] Ebrahimi M, Botelho MG, Dorozhkin SV. Biphasic calcium phosphates bioceramics (HA/TCP): Concept, physicochemical properties and the impact of standardization of study protocols in biomaterials research. Mater Sci Eng, C. 2017;71:711293–312. doi: 10.1016/j. msec.2016.11.039.
- [11] Lee SW, Kim Y, Rho HT, Kim S-I. Microhardness and microstructural properties of a mixture of hydroxyapatite and β-tricalcium phosphate. J Asian Ceram Soc. 2023;11(1):11–7. doi: 10.1080/21870764. 2022.2136261.
- [12] Hou X, Zhang L, Zhou Z, Luo X, Wang T, Zhao X, et al. Calcium phosphate-based biomaterials for bone repair. J Funct Biomater. 2022;13(4):187. doi: 10.3390/jfb13040187.
- [13] Nevado P, Lopera A, Bezzon V, Fulla M, Palacio J, Zaghete M, et al. Preparation and in vitro evaluation of PLA/biphasic calcium phosphate filaments used for fused deposition modelling of scaffolds. Mater Sci Eng, C. 2020;114:114111013. doi: 10.1016/j.msec.2020. 111013.
- [14] Gan D, Liu M, Xu T, Wang K, Tan H, Lu X. Chitosan/biphasic calcium phosphate scaffolds functionalized with BMP-2-encapsulated nanoparticles and RGD for bone regeneration. J Biomed Mater Res Part A. 2018;106(10):2613–24. doi: 10.1002/jbm.a.36453.
- [15] Cheng Y, Morovvati M, Huang M, Shahali M, Saber-Samandari S, Angili SN, et al. A multilayer biomimetic chitosan-gelatin-fluorohydroxyapatite cartilage scaffold using for regenerative medicine

- application. J Mater Res Technol. 2021;14:141761–77. doi: 10.1016/j.jmrt.2021.07.052.
- [16] Abd-Khorsand S, Saber-Samandari S, Saber-Samandari S. Development of nanocomposite scaffolds based on TiO2 doped in grafted chitosan/hydroxyapatite by freeze drying method and evaluation of biocompatibility. Int J Biol Macromol. 2017;101:10151–8. doi: 10.1016/j.ijbiomac.2017.03.067.
- [17] Sendemir-Urkmez A, Jamison RD. The addition of biphasic calcium phosphate to porous chitosan scaffolds enhances bone tissue development *in vitro*. J Biomed Mater Res Part A. 2007;81(3):624–33. doi: 10.1002/jbm.a.31010.
- [18] Kardan-Halvaei M, Morovvati M, Angili SN, Saber-Samandari S, Razmjooee K, Toghraie D, et al. Fabrication of 3D-printed hydroxyapatite using freeze-drying method for bone regeneration: RVE and finite element simulation analysis. J Mater Res Technol. 2023;24:248682–92. doi: 10.1016/j.jmrt.2023.05.099.
- [19] El-Gohary M, El-Dyn S, Abd El-moniem B, Al-Ashkar E, Saleh E, Tolba E, et al. Synthesis and microstructure characterization of novel Sr-HA prepared by co-precipitation with enhanced bioactivity. Egypt J Biophys Biomed Eng. 2012;13:1373–85. doi: 10.21608/ ejbbe.2012.1194.
- [20] Priyadarshini I, Swain S, Koduru JR, Rautray TR. Electrically polarized withaferin a and alginate-incorporated biphasic calcium phosphate microspheres exhibit osteogenicity and antibacterial activity in vitro. Molecules. 2022;28(1):86. doi: 10.3390/molecules28010086.
- [21] Park K, Kim S, Hwang M, Song H, Park Y. Biomimetic fabrication of calcium phosphate/chitosan nanohybrid composite in modified simulated body fluids. Exp Polym Lett. 2017;11(1):14. doi: 10.3144/ expresspolymlett.2017.3.
- [22] Kokubo T, Takadama H. How useful is SBF in predicting in vivo bone bioactivity? Biomater. 2006;27(15):2907–15. doi: 10.1016/j. biomaterials.2006.01.017.
- [23] Tohamy KM, Mabrouk M, Soliman IE, Beherei HH, Aboelnasr MA. Novel alginate/hydroxyethyl cellulose/hydroxyapatite composite scaffold for bone regeneration: In vitro cell viability and proliferation of human mesenchymal stem cells. Int J Biol Macromol. 2018;112:112448–60. doi: 10.1016/j.ijbiomac.2018.01.181.
- [24] Tuorkey M, Khedr Y, Aborhyem S, Xue X. Green synthesis of chicory (Cichorium intybus L.) Chitosan nanoparticles and evaluation of their anti-fungal, anti-hemolytic, and anti-cancer activities. J Bioact Compat Polym. 2022;37(6):421–36. doi: 10.1177/08839115221126737.
- [25] Karava A, Lazaridou M, Nanaki S, Michailidou G, Christodoulou E, Kostoglou M, et al. Chitosan derivatives with mucoadhesive and antimicrobial properties for simultaneous nanoencapsulation and extended ocular release formulations of dexamethasone and chloramphenicol drugs. Pharmaceutics. 2020;12(6):594. doi: 10. 3390/pharmaceutics12060594.
- [26] El-Meliegy E, Abu-Elsaad N, El-Kady AM, Ibrahim MA. Improvement of physico-chemical properties of dextran-chitosan composite scaffolds by addition of nano-hydroxyapatite. Sci Rep. 2018;8(1):1–10.
- [27] Ji Yin Y, Zhao F, Feng Song X, De Yao K, Lu WW, Chiyan Leong J. Preparation and characterization of hydroxyapatite/chitosan–gelatin network composite. J Appl Polym Sci. 2000;77(13):2929–38. doi: 10.1002/1097-4628(20000923)77:13.
- [28] Langford J. X-ray diffraction procedures for polycrystalline and amorphous materials by HP Klug and LE Alexander. J Appl Crystallogr. 1975;8(5):573–4. doi: 10.1107/S0021889875011399.

- [29] El-Sherbiny IM, Yahia S, Messiery MA, Reicha FM. Preparation and physicochemical characterization of new nanocomposites based on β-type chitosan and nano-hydroxyapatite as potential bone substitute materials. Int J Polym Mater Polym Biomater. 2014;63(4):213-20. doi: 10.1080/00914037.2013.830249.
- [30] Landi E, Tampieri A, Celotti G, Sprio S. Densification behaviour and mechanisms of synthetic hydroxyapatites. J Eur Ceram Soc. 2000;20(14-15):2377-87. doi: 10.1016/S0955-2219(00)00154-0.
- [31] Zhang Y, Venugopal JR, El-Turki A, Ramakrishna S, Su B, Lim CT. Electrospun biomimetic nanocomposite nanofibers of hydroxyapatite/chitosan for bone tissue engineering. Biomater. 2008;29(32):4314-22. doi: 10.1016/j.biomaterials.2008.07.038.
- [32] Xianmiao C, Yubao L, Yi Z, Li Z, Jidong L, Huanan W. Properties and in vitro biological evaluation of nano-hydroxyapatite/chitosan membranes for bone guided regeneration. Mater Sci Eng, C. 2009;29(1):29-35. doi: 10.1016/j.msec.2008.05.008.
- [33] Vecstaudza J, Gasik M, Locs J. Amorphous calcium phosphate materials: Formation, structure and thermal behaviour. | Eur Ceram Soc. 2019;39(4):1642-9. doi: 10.1016/j.jeurceramsoc.2018. 11.003.
- [34] Meng L, Xie F, Zhang B, Wang DK, Yu L. Natural biopolymer alloys with superior mechanical properties. ACS Sustain Chem Eng. 2018;7(2):2792-802. doi: 10.1021/acssuschemeng.8b06009.
- [35] Mohandes F, Salavati-Niasari M. Freeze-drying synthesis, characterization and in vitro bioactivity of chitosan/graphene oxide/ hydroxyapatite nanocomposite. RSC Adv. 2014;4(49):25993-6001. doi: 10.1039/C4RA03534H.
- Raz M, Moztarzadeh F, Kordestani SS. Synthesis, characterization and in-vitro study of chitosan/gelatin/calcium phosphate hybrid scaffolds fabricated via ion diffusion mechanism for bone tissue engineering. Silicon. 2018;10:10277-86. doi: 10.1007/s12633-016-
- [37] Eivazzadeh-Keihan R, Pajoum Z, Aliabadi HAM, Mohammadi A, Kashtiaray A, Bani MS, et al. Magnetized chitosan hydrogel and silk fibroin, reinforced with PVA: a novel nanobiocomposite for biomedical and hyperthermia applications. RSC Adv. 2023;13(13):8540-50. doi: 10.1039/D3RA00612C.
- [38] Mauricio-Sánchez RA, Salazar R, Luna-Bárcenas JG, Mendoza-Galván A. FTIR spectroscopy studies on the spontaneous neutralization of chitosan acetate films by moisture conditioning. Vib Spectrosc. 2018;94:941-6. doi: 10.1016/j.vibspec.2017.10.005.
- [39] Radwan NH, Nasr M, Ishak RA, Abdeltawab NF, Awad GA. Chitosancalcium phosphate composite scaffolds for control of post-operative osteomyelitis: Fabrication, characterization, and in vitro-in vivo evaluation. Carbohydr Polym. 2020;244:244116482. doi: 10.1016/j. carbpol.2020.116482.
- [40] Carvalho GK, Farias JR, Lima IS, Nascimento AM, Neves GA, Menezes R, et al. HAp/β-TCP Biphasic ceramics obtained by the pechini method: An antibacterial approach. Minerals. 2022;12(12):1482. doi: 10.3390/min12121482.
- [41] Weiner S, Bar-Yosef O. States of preservation of bones from prehistoric sites in the Near East: a survey. J Archaeol Sci: Rep. 1990;17(2):187-96. doi: 10.1016/0305-4403(90)90058-D.
- [42] Thein-Han W, Misra R. Biomimetic chitosan-nanohydroxyapatite composite scaffolds for bone tissue engineering. Acta Biomater. 2009;5(4):1182-97. doi: 10.1016/j.actbio.2008.11.025.
- [43] El-Sayed SA, Mabrouk M, Khallaf ME, Abd El-Hady BM, El-Meliegy E, Shehata MR. Antibacterial, drug delivery, and osteoinduction abilities of bioglass/chitosan scaffolds for dental applications.

- J Drug Deliv Sci Technol. 2020;57:57101757. doi: 10.1016/j.jddst. 2020.101757.
- [44] Ersal F, Sari Y. Synthesis and characterization of hydroxyapatite-chitosan composite in situ by microwave irradiation method. J Phys: Conf Ser. 2019;1248(1):012080. doi: 10.1088/1742-6596/1248/1/012080.
- [45] Chen J, Zhang G, Yang S, Li J, Jia H, Fang Z, et al. Effects of in situ and physical mixing on mechanical and bioactive behaviors of nano hydroxyapatite-chitosan scaffolds. I Biomater Sci. Polym Ed. 2011;22(15):2097-106. doi: 10.1163/092050610X533691.
- [46] Peter M, Ganesh N, Selvamurugan N, Nair S, Furuike T, Tamura H, et al. Preparation and characterization of chitosan-gelatin/nanohydroxyapatite composite scaffolds for tissue engineering applications. Carbohydr Polym. 2010;80(3):687-94. doi: 10.1016/j. carbpol.2009.11.050.
- [47] Leonor IB, Baran ET, Kawashita M, Reis R, Kokubo T, Nakamura T. Growth of a bonelike apatite on chitosan microparticles after a calcium silicate treatment. Acta Biomater. 2008;4(5):1349-59. doi: 10.1016/j.actbio.2008.03.003.
- [48] Luz GM, Mano JF. Chitosan/bioactive glass nanoparticles composites for biomedical applications. Biomed Mater. 2012;7(5):054104. doi: 10.1088/1748-6041/7/5/054104.
- [49] Nguyen TP, Tran NQ. Preparation and biomineralization of injectable hydrogel composite based chitosan-tetronic and bcp nanoparticles. Adv Res. 2016;7:71-8. doi: 10.9734/AIR/2016/25891.
- Jayash SN, Cooper PR, Shelton RM, Kuehne SA, Poologasundarampillai G. Novel chitosan-silica hybrid hydrogels for cell encapsulation and drug delivery. Int | Mol Sci. 2021;22(22):12267. doi: 10.3390/ijms222212267.
- [51] Li B, Xia X, Guo M, Jiang Y, Li Y, Zhang Z, et al. Biological and antibacterial properties of the micro-nanostructured hydroxyapatite/chitosan coating on titanium. Sci Rep. 2019;9(1):14052. doi: 10.1038/s41598-019-49941-0.
- [52] Yamashita K, Oikawa N, Umegaki T. Acceleration and deceleration of bone-like crystal growth on ceramic hydroxyapatite by electric poling. Chem Mater. 1996;8(12):2697-700. doi: 10.1021/cm9602858.
- [53] Zheng K, Wu Z, Wei J, Rűssel C, Liang W, Boccaccini AR. Preparation and characterization of fibrous chitosan-glued phosphate glass fiber scaffolds for bone regeneration. J Mater Sci Mater Med. 2015;26:261-10. doi: 10.1007/s10856-015-5554-8.
- [54] Soliman IE-S, Metawa AE-S, Aboelnasr MAH, Eraba KT, Surface treatment of sol-gel bioglass using dielectric barrier discharge plasma to enhance growth of hydroxyapatite. Korean J Chem Eng. 2018;35:352452-63. doi: 10.1007/s11814-018-0131-8.
- [55] Elhendawi H, Felfel R, El-Hady A, Bothaina M, Reicha FM. Effect of synthesis temperature on the crystallization and growth of in situ prepared nanohydroxyapatite in chitosan matrix. Int Sch Res Notices. 2014;2014:1-8. doi: 10.1155/2014/897468.
- Garskaite E, Gross K-A, Yang S-W, Yang TC-K, Yang J-C, Kareiva A. [56] Effect of processing conditions on the crystallinity and structure of carbonated calcium hydroxyapatite (CHAp). Cryst Eng Comm. 2014;16(19):3950-9. doi: 10.1039/C4CE00119B.
- [57] Teimouri A, Azadi M. Preparation and characterization of novel chitosan/nanodiopside/nanohydroxyapatite composite scaffolds for tissue engineering applications. Int J Polym Mater Polym Biomater. 2016;65(18):917-27. doi: 10.1080/00914037.2016.1180606.
- [58] Maji K, Dasgupta S. Characterization and in vitro evaluation of gelatin-chitosan scaffold reinforced with bioceramic nanoparticles for bone tissue engineering. | Mater Res. 2019;34(16):2807-18. doi: 10.1557/jmr.2019.170.

16

- [59] Lü X, Zhang H, Huang Y, Zhang Y. A proteomics study to explore the role of adsorbed serum proteins for PC12 cell adhesion and growth on chitosan and collagen/chitosan surfaces. Regener Biomater. 2018;5(5):261–73. doi: 10.1093/rb/rby017.
- [60] Abueva CD, Padalhin AR, Min Y-K, Lee B-T. Preformed chitosan cryogel-biphasic calcium phosphate: A potential injectable biocomposite for pathologic fracture. J Biomater Appl. 2015;30(2):182–92. doi: 10.1177/0885328215577892.
- [61] Dantas MJ F, dos Santos BF A, Tavares A, Maciel MA, Lucena BdM L, Fook MV, et al. The impact of the ionic cross-linking mode on the physical and in vitro dexamethasone release properties o-f chitosan/hydroxyapatite beads. Molecules. 2019;24(24):4510. doi: 10.3390/molecules242444510.
- [62] Zhang Y, Zhang M. Synthesis and characterization of macroporous chitosan/calcium phosphate composite scaffolds for tissue engineering. J Biomed Mater Res. 2001;55(3):304–12. doi: 10.1002/1097-4636(20010605)55:3 < 304: AID-JBM1018 > 3.0.CO;2-J.
- [63] Hammad HG, Salama MNF. Porosity pattern of 3D chitosan/ bioactive glass tissue engineering scaffolds prepared for bone regeneration. Open Dent J. 2021;15(1):41–56. doi: 10.2174/ 1874210602115010041.
- [64] El Gohary M, El-Din S, Awad S, El-Tohamy AM, Soliman I. Influence of Li 2 content on formation of apatite layer on surface of SiO₂-CaO-K₂O-P₂O₅ bioglass system. Egypt J Biophys Biomed Eng. 2012;13(1):37–52. doi: 10.21608/EJBBE.2012.1192.

- [65] d'Arros C, Rouillon T, Veziers J, Malard O, Borget P, Daculsi G. Bioactivity of biphasic calcium phosphate granules, the control of a needle-like apatite layer formation for further medical device developments. Front Bioeng Biotechnol. 2020;7:7462. doi: 10.3389/ fbioe.2019.00462.
- [66] Eliaz N, Metoki N. Calcium phosphate bioceramics: a review of their history, structure, properties, coating technologies and biomedical applications. Materials. 2017;10(4):334. doi: 10.3390/ma10040334.
- [67] Jahan K, Manickam G, Tabrizian M, Murshed M. In vitro and in vivo investigation of osteogenic properties of self-contained phosphatereleasing injectable purine-crosslinked chitosan-hydroxyapatite constructs. Sci Rep. 2020;10(1):1–17. doi: 10.1038/s41598-020-67886-7.
- [68] Cai B, Zou Q, Zuo Y, Li L, Yang B, Li Y. Fabrication and cell viability of injectable n-HA/chitosan composite microspheres for bone tissue engineering. RSC Adv. 2016;6(89):85735–44. doi: 10.1039/ C6RA06594F.
- [69] Park J-C, Lim H-C, Sohn J-Y, Yun J-H, Jung U-W, Kim C-S, et al. Bone regeneration capacity of two different macroporous biphasic calcium materials in rabbit calvarial defect. J Korean Acad Periodontol. 2009;39(Suppl):223–30. doi: 10.5051/jkape.2009.39.S.223.
- [70] Krithiga G, Jena A, Selvamani P, Sastry T. In vitro study on biomineralization of biphasic calcium phosphate biocomposite crosslinked with hydrolysable tannins of Terminalia chebula. Bull Mater Sci. 2011;34:34589–94. doi: 10.1007/s12034-011-0075-7.